Advanced Powder Technology 37 (2026) 105304

Contents lists available at ScienceDirect

Advanced Powder Technology

journal homepage: www.elsevier.com/locate/apt

Original Research Paper

Prompt-guided zero-shot Depth-aware transformer pipeline for democratized SEM particle characterization: A case study in battery materials

Ahmed Eisa [a,*], Mayank Gupta [b], Alex Kong [c], Finn Frankenberg [a], Maximilian Kissel [d], Dimitri Ivanov [a], Kostas Giannis [a], Carsten Schilde [a]

[a] Institute for Particle Technology (iPAT), Technische Universität Braunschweig, Volkmaroder Str. 5, D-38104 Braunschweig, Germany
[b] Indian Institute of Technology Bombay, Academic Section, IIT Area, Mumbai 400076, Maharashtra, India
[c] University of Quebec in Outaouais, 283 Alexandre-Taché Blvd, Quebec J8X 3X7, Canada
[d] Justus Liebig University Gießen, Ludwigstraße 23, 35390 Gießen, Germany

ARTICLE INFO

Article history:
Received 12 December 2025
Received in revised form 3 April 2026
Accepted 12 May 2026

Keywords:
Particle characterization
Interactive segmentation
Particle surface roughness
Solidstate batteries

ABSTRACT

Microscopy-based particle characterization tools fail on complex images, produce fixed uncorrectable outputs, and lack integrated size, shape, and surface analysis; comprehensive solutions remain commercial or instrument-dependent, with no open-source alternative. This work presents IPGSS (Interactive Prompt-Guided Segmentation System) and DRCS (Depth-based Roughness Characterization System), a training-free pipeline built on open-source vision models for comprehensive particle characterization from standard microscopy images without specialized instrumentation. IPGSS combines zero-shot segmentation, hierarchical post-processing, and interactive correction; DRCS extracts ISO-compliant roughness from a single SEM image. Certified 390 μm polystyrene particles validated accuracy at equivalent circular diameter D_{50} = 388.8 μm (−0.3%). On complex aluminum oxide images, number-weighted D_{50} = 49.9 μm (−0.2%) and volume-weighted D_{90} matched QICPIC within 0.4–4% across >9,000 particles; IPGSS outperformed OpenCV and Cellpose. DRCS replaces the tilt-series approach of Hülagü et al. (2024) with two tracks from a single zero-tilt SEM image. The contour track achieved Spearman r = 0.983 (RMSE = 1.48 nm for near-spherical particles; 96.3% concordant pairs); the depth track provided 3D descriptors including a coating classifier that separated coated from uncoated nanoparticles with zero overlap. A ~20 nm noise floor caused roughness overestimation, though between-type ordering was preserved. IPGSS resolved primary particles (D_{50} = 0.54 μm) within solid-state battery agglomerates measured by laser diffraction at 9.47 μm, a 17.5-fold discrepancy critical for electrode design.

1. Introduction

Particle characterization is fundamental to understanding and controlling the properties of particulate materials across diverse applications including pharmaceuticals, ceramics, energy storage, and advanced manufacturing [1,2]. Conventional measurement techniques such as laser diffraction, sieve analysis, and dynamic image analysis provide quantitative assessment of particle size distributions (PSDs) and morphological properties, yet encounter significant limitations when analyzing complex samples containing overlapping particles, agglomerates, or heterogeneous surfaces [3,4]. In particular, laser diffraction measures agglomerates rather than primary particles and requires dispersion media that may alter material properties, while sieve analysis cannot capture morphological information. Microscopy-based image analysis offers a compelling alternative by enabling direct observation of individual particle boundaries and morphologies, but the extraction of quantitative data from such images remains a persistent bottleneck.

Traditional computer vision approaches for particle segmentation employ classical algorithms including threshold-based methods [5], edge detection, and watershed segmentation [6,7]. While effective for well-separated particles with uniform contrast, these

* Corresponding author.
E-mail addresses: ahmed.eisa@tu-braunschweig.de (A. Eisa), 210101002@iitb.ac.in (M. Gupta), kona39@uqo.ca (A. Kong), finn.frankenberg@tu-braunschweig.de (F. Frankenberg), maximilian.kissel@pc.jlug.de (M. Kissel), d.ivanov@tu-braunschweig.de (D. Ivanov), k.giannis@tu-braunschweig.de (K. Giannis), c.schilde@tu-braunschweig.de (C. Schilde).

https://doi.org/10.1016/j.apt.2026.105304
0921-8831/

methods systematically fail on complex microscopy images featuring touching particles, varying illumination, and textured backgrounds. Deep learning has emerged as an alternative, with architectures such as U-Net [8] and Mask R-CNN [9] demonstrating improved segmentation performance. Cellpose [10], a generalist deep learning model trained on diverse biological microscopy datasets, represents the current state of the art for cellular and particulate segmentation. However, these approaches share fundamental limitations: they require domain-specific training datasets, struggle to generalize across different particle systems and imaging conditions, and critically, produce fixed outputs with no mechanism for the user to correct errors.

Vision foundation models, trained on massive datasets, have recently demonstrated remarkable zero-shot generalization to specialized domains [11]. The Segment Anything Model (SAM) [12], built on vision transformer (ViT) architectures [13,14], achieves state-of-the-art interactive segmentation without domain-specific training. Several studies have begun applying SAM to microscopy: μSAM [15] fine-tunes SAM for biological light and electron microscopy, NP-SAM [16] explores zero-shot nanoparticle segmentation with post-filtering, and Monteiro et al. [17] demonstrate SAM-based morphological characterization of subdivided nanoparticles with size discrepancies below 2%. Uncertainty-aware Mask R-CNN approaches have also been proposed for scanning electron microscopy (SEM) particle analysis at varied length scales [18]. However, these works address segmentation in isolation: none provide integrated quantitative particle characterization with ISO-compliant size, shape, and surface analysis; none offer interactive post-segmentation correction where the user can refine the model's output; and none validate against both certified reference standards and industrial measurement systems.

Surface roughness characterization represents another critical dimension of particle analysis, traditionally requiring specialized instrumentation such as atomic force microscopy (AFM) or stylus profilometry. AFM provides nanometer-scale resolution but is limited to localized surface regions, requires complex sample preparation, and demands significant operator expertise [19]. Monocular depth estimation using dense prediction transformers (DPT) [20,21] has emerged as a computer vision technique for 3D reconstruction from single images, with zero-shot generalization across diverse domains. This capability has not previously been applied to particle surface roughness quantification.

This work presents the Interactive Prompt-Guided Segmentation System (IPGSS), a unified transformer-based pipeline for particle characterization that addresses these gaps through several contributions. First, we combine zero-shot SAM segmentation (supporting both SAM 1 ViT-H and SAM 2.1 Hiera architectures) with a hierarchical post-processing cascade that achieves accurate particle identification across diverse imaging conditions without domain-specific training or manual parameter tuning. Second, we introduce a hybrid workflow in which automatic segmentation results can be interactively refined. This interactive post-segmentation refinement is, to the authors' knowledge, novel in particle characterization and addresses the fundamental limitation of existing tools that produce fixed, uncorrectable outputs. Third, the IPGSS computes ISO-compliant size and shape metrics (ISO 9276–6 [22], ISO 13322–1 [23]) alongside depth-based surface roughness parameters (ISO 4287/4288 [24,25]) from standard SEM images via DRCS, enabling comprehensive characterization without specialized instrumentation or multi-image tilt-series acquisition. Fourth, measurement accuracy is validated against certified 390 μm polystyrene standard particles and QICPIC dynamic image analysis [26] under both dispersed and dry preparation conditions, with statistical adequacy evaluated following Masuda and Gotoh [27] and Matsuyama [28]. Finally, a solid-state battery (SSB) case study demonstrates the pipeline's ability to resolve primary particles within agglomerated structures that conventional laser diffraction cannot distinguish. The IPGSS workflow and all measurement formulas are illustrated in Fig. 1.

2. Methodology

2.1. Materials and sample preparation

For size and shape validation, aluminum oxide samples (Noxid Pulver-160, Final GmbH, 99.8% purity, $D_{50} \approx 50$ μm) were prepared under two conditions designed to generate images of increasing segmentation complexity. In the dispersed condition, samples were ultrasonicated in water for 5 min at room temperature using standardized power settings to ensure reproducible dispersion without particle fracture. Suspensions were deposited by calibrated micropipette drop-casting and imaged with a WITec alpha300 R optical microscope under standardized settings. In the dry condition, powder was gently spread on glass slides to form a monolayer, yielding images with touching particles, complex backgrounds, overlapping boundaries, and varying contrast. Reference distributions were obtained in parallel with a QICPIC dynamic image analysis system (Sympatec, Germany) operated according to ISO 13322–2 [29], with three repeat runs per condition providing statistically robust ground truth: approximately 950,000 particles per run under dispersed conditions (three runs of 935,000–965,000) and 217,000–934,000 per run under dry conditions (three runs; higher variability due to dry feed rate). Note that the IPGSS operates on any calibrated microscopy image; the aluminum oxide size and shape validation used optical microscopy, while the standard particle accuracy validation and the DRCS surface roughness validation used SEM.

For measurement accuracy validation, certified polystyrene (PS) size standard particles (PS/Q-ST-L4178, nominal diameter 390 μm, microParticles GmbH, Berlin, Germany [30]) were imaged by scanning electron microscopy under dry conditions. Seven images yielding 107 particles were analyzed to assess deviation from the certified size.

For surface roughness validation, 17 nanoparticles across four types (polystyrene (PS), PS/Fe_3O_4 (polystyrene core with iron oxide shell), PS/Fe_3O_4/SiO_2 synthesis batch 1 (B1), PS/Fe_3O_4/SiO_2 synthesis batch 2 (B2)) were selected from the publicly available SEM dataset of Hülagü et al. [19]; their SEM images served as DRCS input and their tilt-series roughness measurements (Rq values derived by merging contour profiles from 6 to 10 SEM images acquired at multiple tilt angles) served as reference, spanning an approximately tenfold surface roughness range.

For the solid-state battery (SSB) case study, Li_3InCl_6 (LIC) solid electrolyte (SE) was synthesized via a solvent-based route [31] and subsequently comminuted for 8 min at 600 rpm. SEM images of the resulting agglomerated clusters were used to demonstrate the IPGSS's capability to resolve submicron primary particles within agglomerates.

2.2. Segmentation pipeline

Prior to segmentation, the user performs scale calibration by drawing a line along the scale bar and entering its corresponding real-world length, from which the pixel size (μm/px) is computed. The IPGSS uses the Segment Anything Model (SAM) [12] as its core engine, supporting both SAM 1 (ViT-H/16, trained on the SA-1B dataset comprising over 1 billion masks across 11 million images) and SAM 2.1 (Hiera backbone with improved segmentation quality [32]). Both models operate in zero-shot mode without domain-specific fine-tuning. All results presented in this work were obtained using SAM 2.1. The IPGSS implements two complemen-

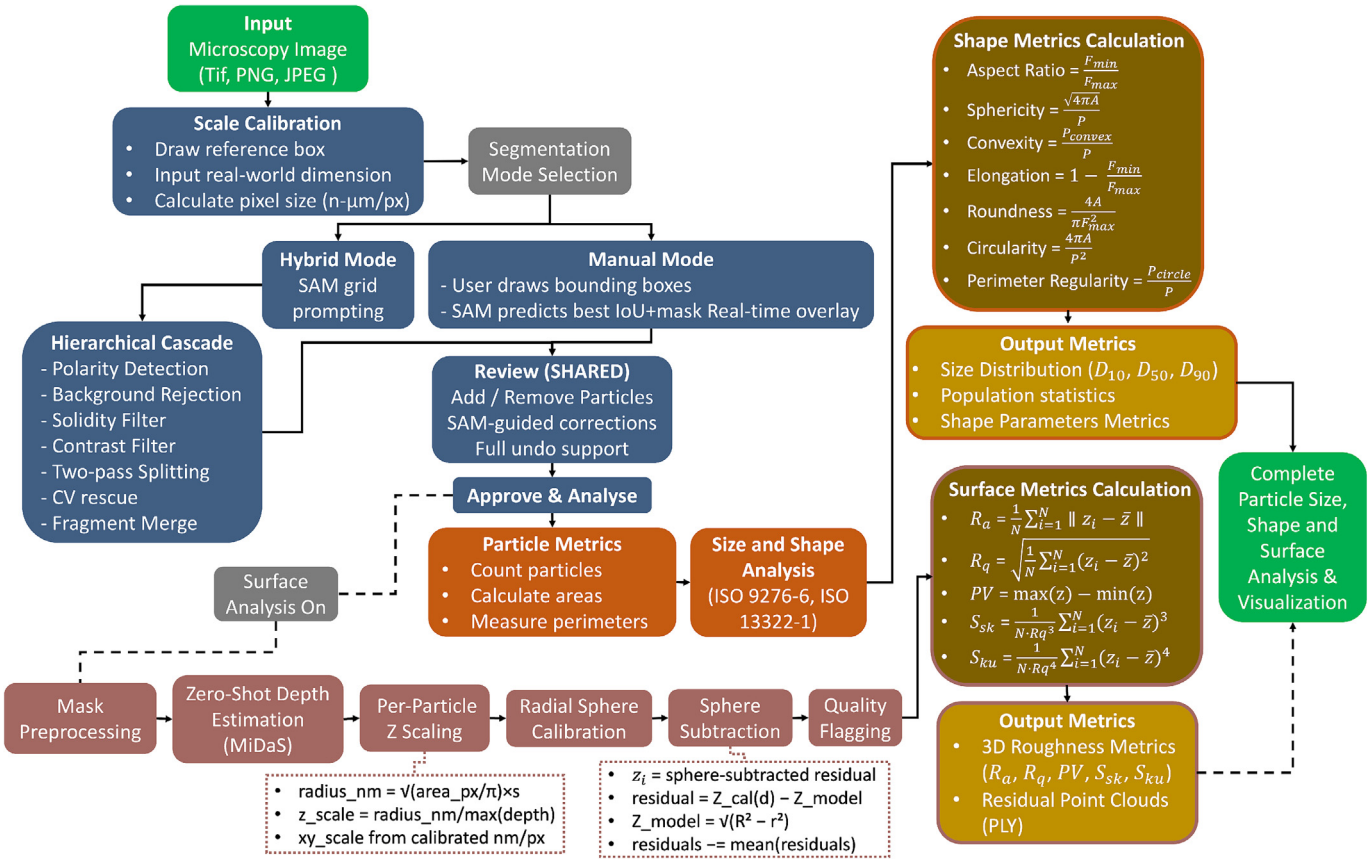

Fig. 1. IPGSS pipeline overview. Microscopy images are calibrated and segmented using SAM/SAM2 in Manual (bounding box) or Hybrid mode (grid prompting with cascade filtering), followed by interactive review. Two parallel branches then run: Size and Shape analysis (ECD, D_{10}/D_{50}/D_{90}, seven ISO 9276–6 shape metrics) and DRCS surface analysis (contour rms_rq from the mask boundary; MiDaS depth estimation with macro-form subtraction yielding hemisphere Rq, surface descriptors and ISO 4287 roughness metrics). All results are exported per particle alongside depth heatmaps and 3D reconstructions.

tary segmentation modes and a shared review step, as illustrated in Fig. 1.

In hybrid mode, SAM automatically generates particle masks across the entire image via grid-based prompting. The raw output passes through a four-stage hierarchical cascade (confidence scoring, area filtering, contrast threshold, and circularity) that rejects artifacts without manual parameter tuning, followed by a two-pass touching-particle separation using adaptive thresholding and distance-transform watershed segmentation, and morphological cleanup. Full algorithmic detail is provided in Supplementary Information Section S2.

In manual mode, the user draws bounding box rectangles directly on the image. For each box, SAM predicts multiple candidate masks and selects the one with the highest intersection-over-union (IoU) confidence score. A real-time overlay provides immediate visual feedback, and full undo support is available.

Both modes converge at a shared review step where the user can interactively add or remove particles. In remove mode, any existing mask with more than 20% overlap with the drawn rectangle is deleted. Manually added masks maintain the same boundary quality as automatically generated ones, since both use SAM's prediction engine.

2.3. Quantitative analysis

Following segmentation approval, the IPGSS computes comprehensive size, shape, and distribution metrics for all detected particles. All calculations follow established ISO standards, with formulas summarized in Table 1.

ECD is equivalent to the equivalent projected circle diameter (EQPC) reported by the QICPIC system [26], enabling direct comparison between static microscopy and dynamic image analysis results.

Particle size distributions are computed following ISO 9276–1 [33] and ISO 9276–2 [34] using four weighting bases: number (Q_0), length (Q_1), area (Q_2), and volume (Q_3). Characteristic percentile diameters D_{10} (10th percentile, fine fraction boundary), D_{50} (50th percentile, median size), and D_{90} (90th percentile, coarse fraction boundary) and the Span is computed as $(D_{90} - D_{10}) / D_{50}$. Three binning methods are provided: Sturges' rule ($k = 1 + 3.322 \times \log_{10}(n)$), square root rule ($k = \sqrt{n}$), and complete distribution (each particle as an individual data point). All distribution plots in this work use Sturges' rule.

Measurement uncertainty follows the analytical framework of Matsuyama [28] for percentile standard deviations and Masuda and Gotoh [27] for minimum required particle count. Expanded uncertainty is reported as $U = 2\sigma$ ($k = 2$, 95% confidence); weighted distributions (Q_1–Q_3) use bootstrap resampling ($B = 5000$). Full formulations are given in Supplementary Information Section S4.

2.4. Depth-based surface roughness analysis

Surface roughness is estimated using the Depth-based Roughness Characterization System (DRCS) from a single standard SEM image with no threshold tuning. DRCS runs two parallel tracks on the same image: a contour track (SAM/SAM2 boundary → rms_rq) and a depth track (MiDaS depth map → hemisphere Rq, sdr/snr, and further descriptors).

Table 1
Measurement parameters and formulas for particle size, shape, and surface roughness characterization. A = particle area, P = perimeter, F_{max} and F_{min} = maximum and minimum Feret diameters, P_{convex} = convex hull perimeter, N = number of surface points, z_i = height of point i, z = mean surface height.

Parameter	Formula	Description
Size Metrics (ISO 9276–6, ISO 13322–1)		
F_{max}	$\max\theta$ [max proj(θ) − min proj(θ)]	Maximum Feret diameter; rotating calipers, 180 directions at 1° steps
F_{min}	$\min\theta$ [max proj(θ) − min proj(θ)]	Minimum Feret diameter; narrowest caliper width
ECD	$2\sqrt{(A / \pi)}$	Equivalent circular diameter; equivalent to QICPIC equivalent projected circle diameter (EQPC)
Shape Metrics (ISO 9276–6), dimensionless, range 0–1		
Aspect Ratio	F_{min} / F_{max}	1 = equiaxed/spherical; →0 = highly elongated
Sphericity	$\sqrt{(4\pi A)} / P$	Circle-equivalent perimeter ratio; 1 = perfect circle
Convexity	P_{convex} / P	Convex hull perimeter ratio; 1 = smooth, <1 = rough
Elongation	$1 - (F_{min} / F_{max})$	0 = equiaxed; →1 = highly elongated
Roundness	$4A / (\pi \times F^2_{max})$	Circle-equivalent area ratio; insensitive to boundary roughness
Circularity	$4\pi A / P2$	Isoperimetric quotient; sensitive to shape and boundary roughness
Perimeter Regularity	P_{circle} / P, $P_{circle} = 2\sqrt{(\pi A)}$	Boundary smoothness; 1 = perfectly smooth circular boundary
Surface Roughness Metrics (ISO 4287/4288)		
R_a	$(1/N)\ \Sigma\lvert z_i - z\rvert$	Arithmetical mean deviation
R_q	$\sqrt{[(1/N)\ \Sigma(z_i - z)^2]}$	Root mean square roughness
PV	$\max(z) - \min(z)$	Peak-to-valley height
S_{sk}	$(1/N{\cdot}R_q^3)\ \Sigma(z_i - z)^3$	Skewness; <0 valley-dominated, >0 peak-dominated
S_{ku}	$(1/N{\cdot}R_q^4)\ \Sigma(z_i - z)^4$	Kurtosis; >3 spiky surface, <3 flat topography

Track 1 – contour roughness. The SAM/SAM2 [12,32] binary mask boundary ∂M is parameterized in polar coordinates centered on the mask centroid, yielding N boundary radii $\{r(\theta_i)\}$ with mean $\bar{r}$. The primary output is the contour root mean square (RMS) roughness: $rms\_rq = \sqrt{[(1/N)\sum(r(\theta_i) - \bar{r})^2]} \times s$, where N is the number of evenly sampled boundary points and s is the pixel scale (nm/px) from SEM metadata. Physically, rms_rq quantifies how much the particle boundary deviates from a perfect circle, capturing surface features that intersect the particle silhouette. This replaces the manual IsoData intensity thresholding of Hülagü et al. [19], which they identified as their most critical uncertainty source. A prospective quality flag is assigned from the mask alone before any roughness value is reported: "non_spherical" (circularity = $4\pi A/P^2$ < 0.80) and "depth_possibly_inverted" (depth gradient inconsistent with expected illumination direction; this arises when a brightness gradient in the SEM image (caused by directional illumination, detector geometry, or local shadowing) is misinterpreted by MiDaS as a lateral depth variation rather than a hemispherical shape, producing a distorted depth map); particles receiving no flag are termed "quality-ok". Bootstrap resampling (B = 200) of the sphere-subtracted depth residuals provides a reference-free uncertainty estimate of hemisphere Rq (bootstrap standard deviation σ_boot).

Track 2 – depth-derived descriptors. The same SEM image is passed to MiDaS (DPT-Large [20,21]) to produce a relative depth map D(x, y). The unitless MiDaS output is linearly rescaled so that the depth range over the particle mask spans [0, d/2] nm, where d is the ECD-derived particle diameter, corresponding to the expected hemisphere height. A second-order polynomial is then fitted by least squares to D(x, y) over the mask and subtracted to isolate surface texture: $D\sim(x, y) = D(x, y) - \hat{D}(x, y)$. The following descriptors are computed from D~: (i) hemisphere Rq: the mean patch-wise RMS roughness over equal-size square patches of the visible hemisphere, reducing projection bias; (ii) depth signal-to-noise ratio snr = Rq / noise_floor, where Rq is the RMS roughness of the sphere-subtracted residuals and noise_floor is the RMS residual from a plane fit to the apex region (top 20% of depth values); high snr = genuine surface structure, not noise; (iii) coating classifier sdr/snr, the ratio of developed surface area ratio Sdr (ISO 25,178 parameter quantifying the fractional increase in true 3D surface area relative to the projected flat area; zero for a perfectly flat surface, larger for rougher surfaces) to snr: large when genuine 3D surface relief exists relative to depth noise, as occurs when a SiO_2 shell deposits over Fe_3O_4 clusters, and small on smooth surfaces where depth variation is noise-dominated; (iv) angular homogeneity: standard deviation of sector-wise Rq across 8 equal azimuthal sectors (45° each), sensitive to coating uniformity; and (v) summit curvature Spc (ISO 25,178 mean principal curvature of surface summits) from D~.

Five ISO 4287/4288-compliant [24,25] roughness parameters (Table 1) are also computed from D~ and exported per particle: Ra, Rq, PV, Ssk, and Sku. These provide additional texture characterization for advanced users; their systematic validation against reference measurements is beyond the scope of the present work.

2.5. Validation framework

The validation strategy encompasses four complementary protocols. First, measurement accuracy is assessed using certified 390 μm polystyrene standard particles, comparing the measured ECD, F_{max}, and F_{min} against the certified diameter. Second, segmentation performance and size distributions are validated against QICPIC reference measurements [26] comprising approximately 950,000 particles per run (dispersed) and up to 934,000 per run (dry), three runs per condition, with Q_3 volume-weighted percentiles compared directly. Third, statistical adequacy is evaluated following Masuda and Gotoh [27] for minimum required particle count and Matsuyama [28] for percentile uncertainty, applied to the combined datasets of 4,857 dry and 4,518 dispersed particles from approximately 100 images in total. Fourth, DRCS contour roughness (rms_rq) is validated against the tilt-series reference of Hülagü et al. [19] on 17 nanoparticles spanning four types (PS, PS/Fe_3O_4, $PS/Fe_3O_4/SiO_2$ B1, B2), using Spearman rank correlation and root mean square error (RMSE) stratified by prospective quality flag, with sdr/snr tested as a coating classifier using known synthesis chemistry as ground truth.

3. Results and Discussion

3.1. Segmentation and particle characterization validation

3.1.1. Segmentation performance comparison

The IPGSS was evaluated on intentionally complex aluminum oxide microscopy images under both dispersed and dry preparation conditions. Comparative analysis was performed against OpenCV [7] edge-based segmentation (representing traditional computer vision) and Cellpose [10] (representing state-of-the-art deep learning trained for microscopy). Representative results are shown in Fig. 2.

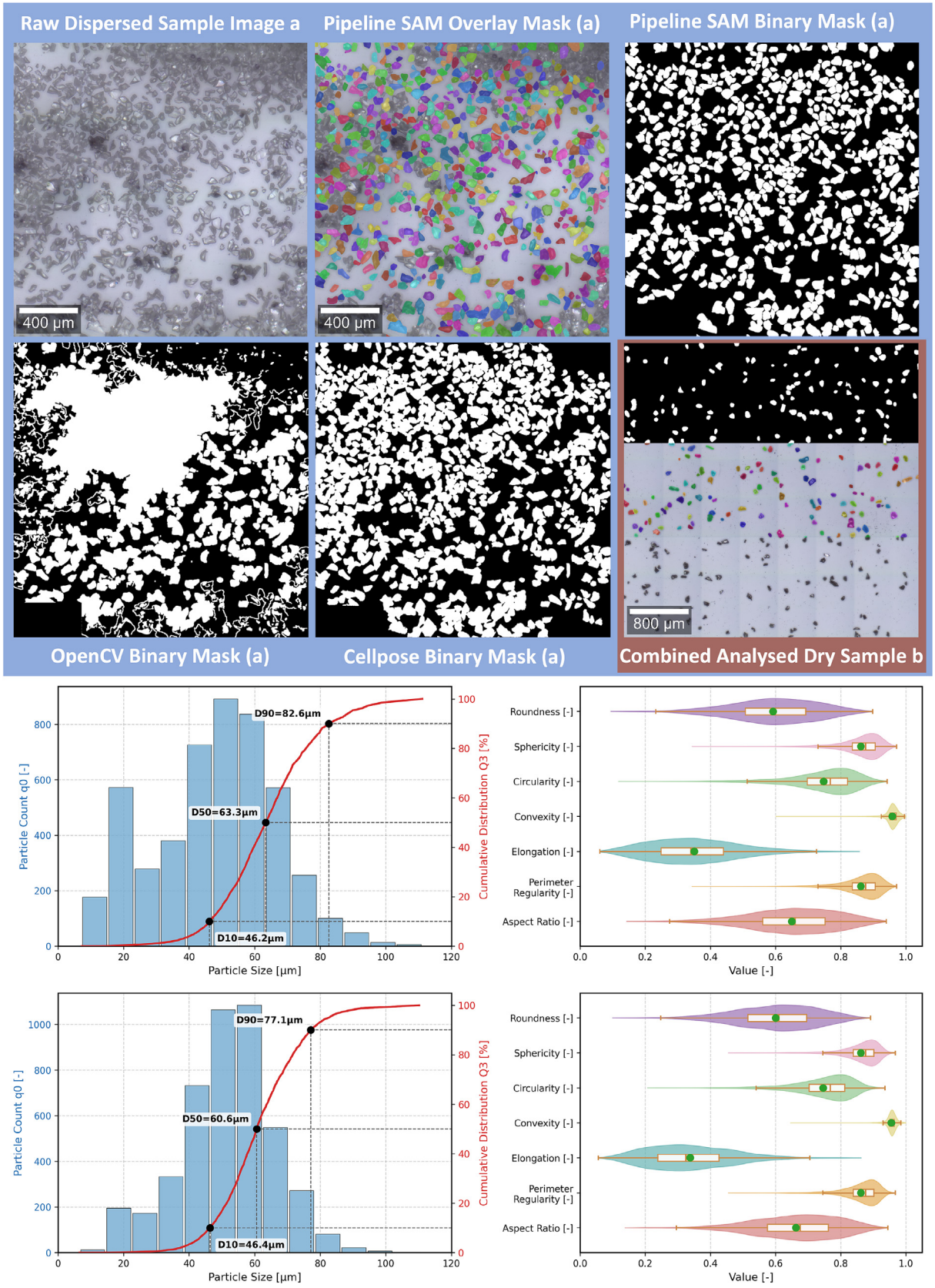

Fig. 2. Segmentation performance and combined analysis results. Top panels: dispersed sample image (a) with SAM overlay, SAM binary mask, OpenCV binary mask, and Cellpose binary mask; dry sample (b) showing segmentation under challenging conditions. Bottom panels: Q_3 volume-weighted frequency histograms and cumulative distributions with D_{10}, D_{50}, and D_{90} annotations for the dry condition (upper row; 4,857 particles, 37 images) and dispersed condition (lower row; 4,518 particles, 64 images), with shape descriptor violin plots.

On dispersed samples, OpenCV produced heavily fragmented boundaries, failing to resolve individual particles in regions of moderate complexity. Cellpose generated more coherent masks but frequently merged adjacent particles into single detections, inflating apparent particle sizes by 25 to 100% relative to QICPIC reference measurements, with errors increasing for closely spaced particles. The IPGSS preserved particle individuality even in challenging regions with touching boundaries and varying contrast, and following interactive review and correction, produced particle counts and size distributions closely matching the QICPIC reference. On dry samples, which exhibit higher complexity due to touching particles, textured backgrounds, and non-uniform illumination, the same performance hierarchy was observed: OpenCV failed systematically, Cellpose merged particles, and the IPGSS, aided by the hierarchical post-processing cascade that removed background false detections and separated touching particles without manual parameter adjustment, resolved individual particles accurately (Fig. 2, top right).

Manual correction of a small number of merged or missed particles per image required only seconds, compared to full re-analysis or re-parameterization needed by conventional tools.

3.1.2. Standard particle accuracy

Measurement accuracy was validated using certified 390 μm polystyrene standard particles (PS/Q-ST-L4178). Analysis of 107 particles across seven SEM images yielded an ECD D50 of 388.8 μm, corresponding to a deviation of −0.3% from the certified value (Fig. 3, bottom panels). The arithmetic mean ECD was 386.8 μm (−0.8%), slightly lower due to a small number of outlier particles (6 of 107 with ECD < 370 μm). The maximum Feret diameter (F_{max} = 390.5 μm) showed even closer agreement at +0.1%, as expected for near-spherical particles. The minimum Feret diameter (F_{min} = 385.0 μm) deviated by −1.3%. The small negative ECD bias is consistent with the fact that ECD is derived from projected area, which is slightly smaller than the circumscribed diameter for non-perfectly-circular projections.

Shape descriptors confirmed the calibration-grade spherical morphology: Aspect Ratio = 0.986 ± 0.008, Roundness = 0.981 ± 0.007, Elongation = 0.014 ± 0.008, and Sphericity = 0.945 ± 0.001. Circularity (0.893 ± 0.003) was notably lower than Roundness, a known artifact of pixel discretization at SEM resolution, where perimeter-based metrics are more sensitive to boundary staircasing than area-based metrics. The extremely narrow size distribution (Span = ~0.03, coefficient of variation (CV) = 2.1%) confirmed the monodisperse character of the standard particles, and the bootstrap D_{50} uncertainty of 0.2% demonstrates the precision achievable even with a modest particle count of 107.

3.1.3. Size and shape validation against QICPIC

The QICPIC dynamic image analysis system provided statistically robust reference measurements based on approximately 950,000 particles per run under dispersed conditions and up to 934,000 per run under dry conditions, three repeat runs each (Fig. 3, top panels). Under dispersed conditions, Q_3 volume-weighted percentiles were D_{10} = 16.6 μm, D_{50} = 46.9 μm, and D_{90} = 77.4 μm. Under dry conditions, a shift toward larger sizes was observed (D_{10} = 42.8 μm, D_{50} = 57.3 μm, D_{90} = 79.7 μm), consistent with reduced agglomerate breakup in dry dispersion.

Combined image analysis of 4,857 dry and 4,518 dispersed particles (approximately 100 images in total) produced Q_3 volume-weighted results in good agreement with the QICPIC reference for the coarse fraction (Fig. 2, bottom panels). For the dry condition, Q_3 D_{90} = 82.6 μm matched the QICPIC value (79.7 μm) within 4%, while for the dispersed condition, Q_3 D_{90} = 77.1 μm matched within 0.4%. The Q_3 D_{50} values showed larger apparent deviations (63.3 vs. 57.3 μm for dry, 60.6 vs. 46.9 μm for dispersed); however, these differences are substantially amplified by volume weighting, which scales with the cube of particle diameter and causes a small number of large particles to dominate the distribution. The D_{10} offset for the dispersed condition (46.4 vs. 16.6 μm) further reflects the pixel resolution limit of microscopy-based analysis, which cannot resolve particles below approximately 10 to 15 pixels, truncating the finest fraction that QICPIC captures down to the submicron range. Number-weighted Q_0 D_{50} was 49.9 μm for the dry condition (−0.2% from the nominal 50 μm) and 52.6 μm for dispersed (+5.2%).

Comparison between conditions revealed that dispersed preparation narrows the PSD (Q_0 Span: 0.689 vs. 1.026 for dry) and shifts the fine fraction coarser (Q_0 D_{10}: 32.6 vs. 18.8 μm), consistent with dispersal reducing agglomeration and freeing the finest fraction. The median size remained similar between conditions (Q_0 D_{50}: 52.6 vs. 49.9 μm). Shape descriptors were virtually identical: Aspect Ratio 0.662 ± 0.132 (dispersed) vs. 0.649 ± 0.138 (dry), Sphericity 0.862 ± 0.060 vs. 0.862 ± 0.065, and Circularity 0.746 ± 0.096 vs. 0.747 ± 0.105. This confirms that the preparation method shifts the PSD without altering the measured particle morphology.

3.1.4. Statistical adequacy

Statistical adequacy was confirmed following Masuda and Gotoh [27] and Matsuyama [28]: both datasets exceed the minimum required particle count by a factor of three or more, D_{10} uncertainties are 2.4% (dry) and 3.4% (dispersed), D_{50} uncertainties are 0.8–1.0%, and D_{90} uncertainties are 1.0–1.1%, and D_{50} shifted by less than 1 μm when 22–43% more data were added. Full calculations are provided in Supplementary Information Section S4.

3.2. Surface roughness validation

DRCS contour roughness (rms_rq) was validated against the tilt-series reference of Hülagü et al. [19] on 17 nanoparticles spanning four types: polystyrene (PS), PS/Fe_3O_4, and core–shell silica (CSS) B1 and B2 (both PS/Fe_3O_4/SiO_2); tilt-series reference roughness range 3.8–39.1 nm. A single zero-tilt SEM image per particle was used with no motorized stage or threshold tuning. Fig. 4 (top) illustrates the full DRCS pipeline for a representative CSS B1 particle (rms_rq = 20.56 nm, reference = 20.8 nm, −1.2% error): the SEM image, SAM mask, MiDaS depth heatmap, and macro-form-subtracted 3D reconstruction are shown across five viewing angles. Fig. 4 (middle) shows a gallery of six representative particles spanning the full roughness range (2.98 to 43.31 nm, a 14.5-fold span); particle-level accuracy, quality flag behavior, and the contrast between the contour and depth tracks across this gallery are discussed in Supplementary Information Section S5.

Validation across all 17 particles yielded Spearman r = 0.983 ($p < 0.001$); 131/136 pairs concordant (96.3%). Type-level mean rms_rq ordering was perfectly preserved (values are means across particles of each type): PS (3.3 nm, n = 3) < PS/Fe_3O_4 (11.0 nm, n = 3) < CSS B1 (24.4 nm, n = 6) < CSS B2 (32.8 nm, n = 5), matching the reference exactly (Fig. 4, bottom left). RMSE was 1.48 nm for quality-ok particles (n = 6, circularity ≥ 0.80) and 2.28 nm for flagged particles (n = 11), while bootstrap standard deviation σ_boot of hemisphere Rq provides a complementary reference-free uncertainty estimate.

DRCS further provides depth-derived descriptors unavailable to contour-only methods. The sdr/snr ratio separated SiO_2-coated from uncoated particles with zero overlap (Fig. 4, bottom right; gap = 0.206; Spearman r = 0.870 against the continuous roughness reference, $p < 0.0001$), robust across pixel scales of 1.9–4.0 nm/px without calibration. This separation is inaccessible to the contour track alone: PS/Fe_3O_4 particles already exhibit elevated rms_rq (mean 11.0 nm) due to Fe_3O_4 surface texture, placing them between smooth PS (3.3 nm) and SiO_2-coated particles (24.4–

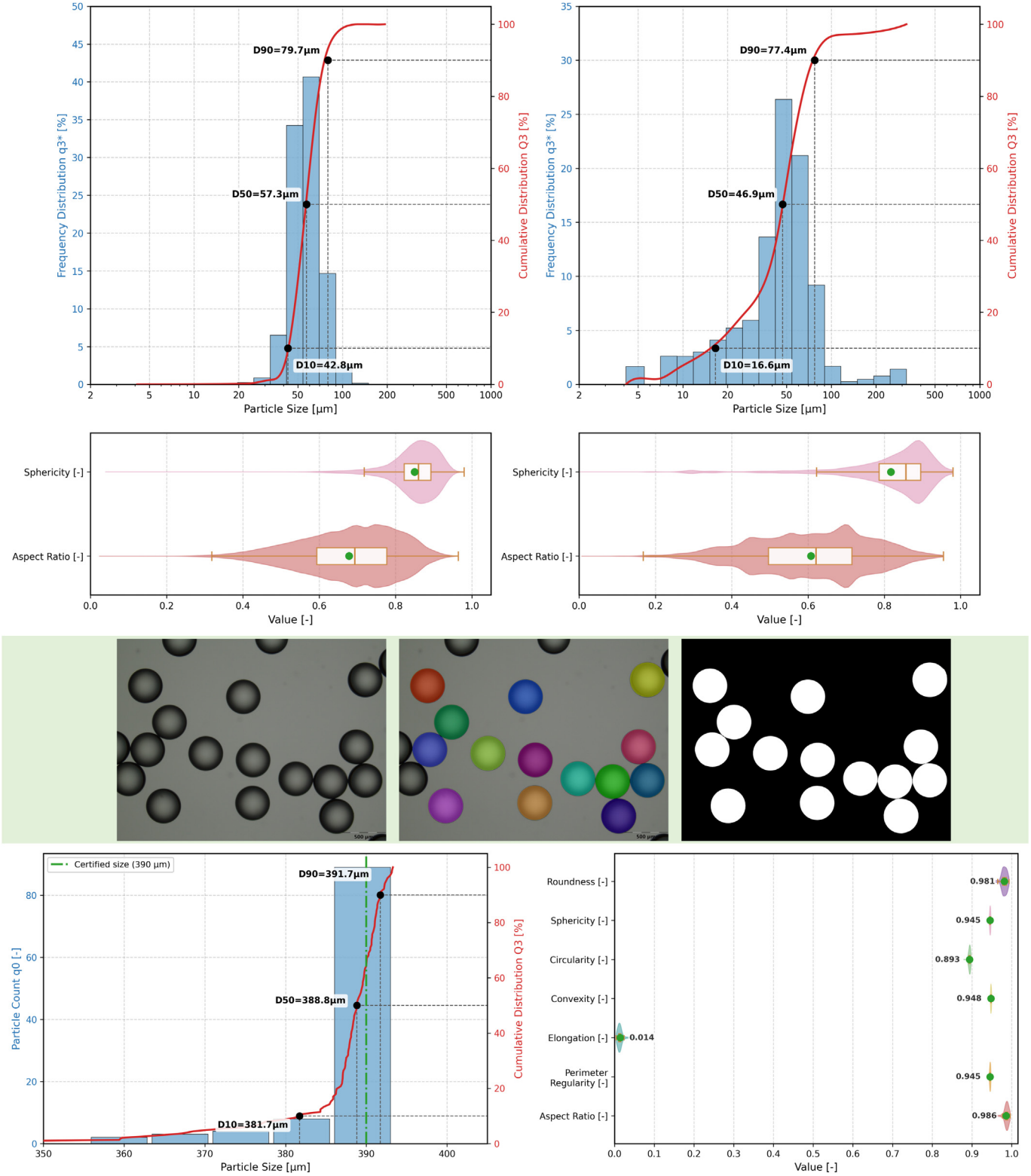

Fig. 3. QICPIC reference measurements and standard particle validation. Top panels: QICPIC reference PSDs under dry and dispersed conditions with Q_3 volume-weighted frequency and cumulative distributions, and sphericity and aspect ratio distributions (~950,000 particles per run (dispersed) and up to 934,000 per run (dry)). Middle panels: raw SEM image, segmentation overlay, and binary mask for representative standard particles. Bottom panels: standard particle PSD with certified 390 µm reference line and shape descriptor violin plots.

32.8 nm) with a narrower and less reliable margin, whereas sdr/snr collapses PS and PS/Fe_3O_4 to near-identical values (2.72 and 2.88) and separates them unambiguously from the coated groups (10.46 and 11.68). This has direct practical relevance for applications such as solid-state battery electrode coatings, where confirming coating presence and uniformity currently requires dedicated instrumentation such as AFM or XPS, whereas sdr/snr offers a rapid screening alternative from routine SEM inspection. Beyond the

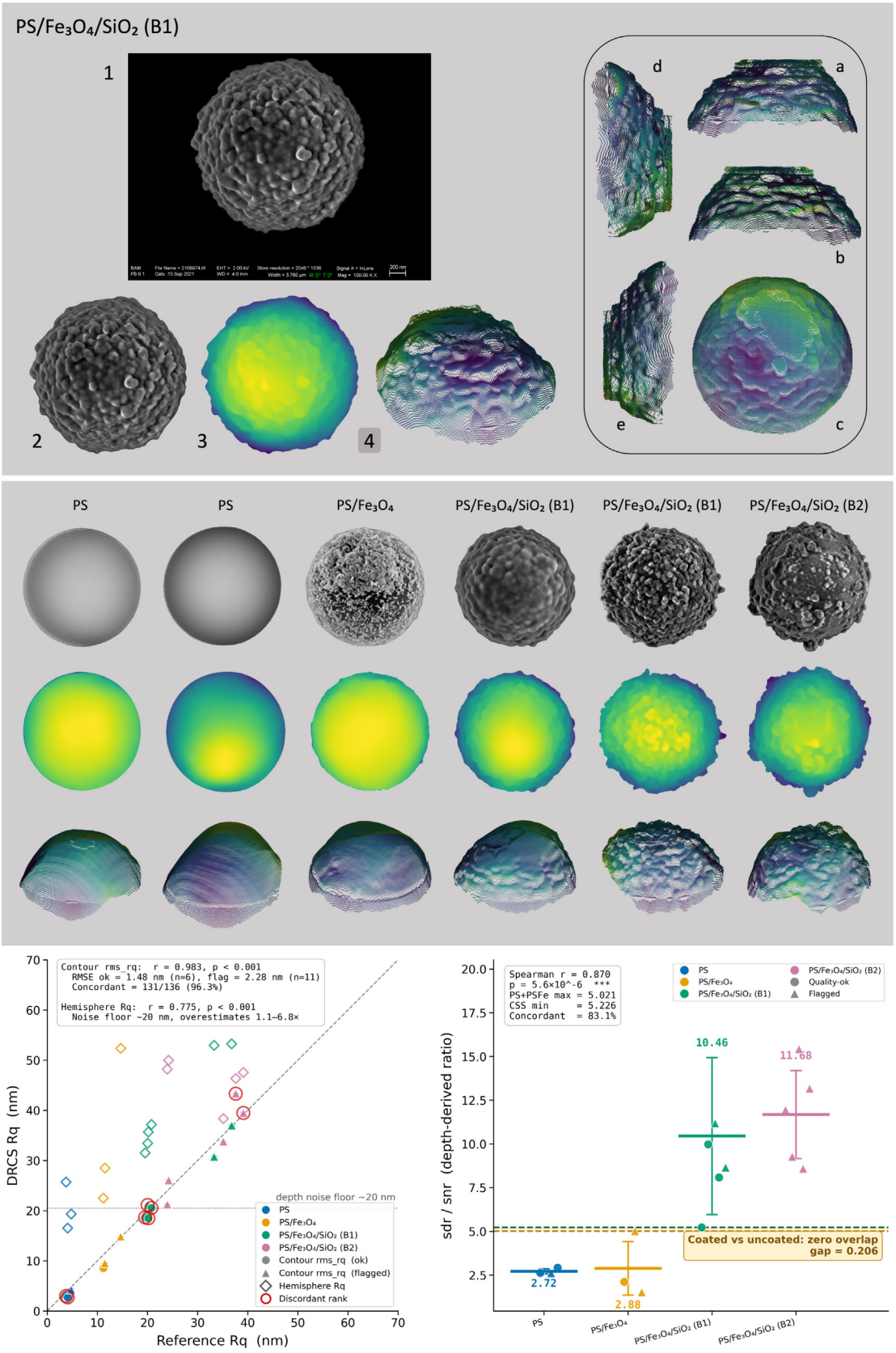

Fig. 4. DRCS surface roughness validation. Top: single particle ($PS/Fe_3O_4/SiO_2$ B1, quality-ok; rms_rq = 20.56 nm, reference = 20.8 nm) showing SEM image, SAM mask, MiDaS depth heatmap, and 3D reconstruction after macro-form subtraction (a–e). Middle: gallery of six particles (PS: one quality-ok, one flagged; PS/Fe_3O_4: one quality-ok; CSS B1: one quality-ok, one flagged; CSS B2: one flagged), spanning the full roughness range (PS ok, 2.98 nm: noise floor dominates hemisphere Rq (6.8×); PS flagged, 4.22 nm: depth_possibly_inverted, contour still usable; PS/Fe_3O_4 ok, 8.55 nm: both tracks perform well; CSS B1 ok, 18.66 nm: representative CSS accuracy; CSS B1 flagged, 30.77 nm: non_spherical boundary; CSS B2 flagged, 43.31 nm: genuine relief reduces overestimation to 1.2×). Circles = quality-ok, triangles = flagged. Bottom left: DRCS rms_rq vs. tilt-series reference Rq for all 17 particles; Spearman r = 0.983; RMSE = 1.48/2.28 nm (quality-ok/flagged); open diamonds = hemisphere Rq. Bottom right: sdr/snr by particle type showing zero-overlap separation between uncoated and SiO_2-coated particles (gap = 0.206; means: PS = 2.72, PS/Fe_3O_4 = 2.88, CSS B1 = 10.46, CSS B2 = 11.68).

coating classifier, the ~20 nm MiDaS noise floor causes hemisphere Rq to overestimate absolute roughness by 1.1–6.8× across all 17 particles. The overestimation is largest for smooth particles (PS: 4.0–6.8×), where depth variation is dominated by noise, and smallest for rough CSS particles (1.1–2.1×), where genuine surface relief partially overcomes the noise floor. Despite this, hemisphere Rq correctly preserves between-type ordering ($r = 0.775$, $p < 0.001$). The mean sector-wise roughness standard deviation (angular homogeneity) was significantly lower for SiO_2-coated than uncoated particles (12.6 ± 5.6 vs 19.9 ± 3.4 nm; one-sided Mann–Whitney $p = 0.007$), and summit curvature Spc declines monotonically across the coating hierarchy (PS/Fe_3O_4: 0.531, CSS B1: 0.376, CSS B2: 0.272; Kruskal–Wallis $p = 0.022$ across the three ordered groups) and further discriminates coating architecture from the same SEM image. These results demonstrate that DRCS enables routine surface roughness characterization and coating detection directly from standard SEM images, with practical applications in quality control of particle coatings, batch consistency monitoring, and correlation of surface texture with functional properties such as dissolution rate, flowability, and electrode performance.

3.3. Solid-state battery application

In SSB development, composite cathodes demand tailored particle size distributions for both the active material and the solid electrolyte (SE) to achieve a functional microstructure [35,36]. The SE PSD often needs to be adapted via comminution and requires corresponding quality control. Conventional laser diffraction faces fundamental challenges in this context: agglomerates are measured instead of primary particles [37–39]; identifying a truly inert solvent for wet dispersion is difficult, since any reaction with the electrolyte can alter its morphology and shift its apparent PSD [40,41]; dry laser diffraction is problematic because many SEs are air- and moisture-sensitive; and particle morphology, which significantly impacts electrode microstructure and electrochemical performance [31,42,43], is entirely inaccessible to laser diffraction.

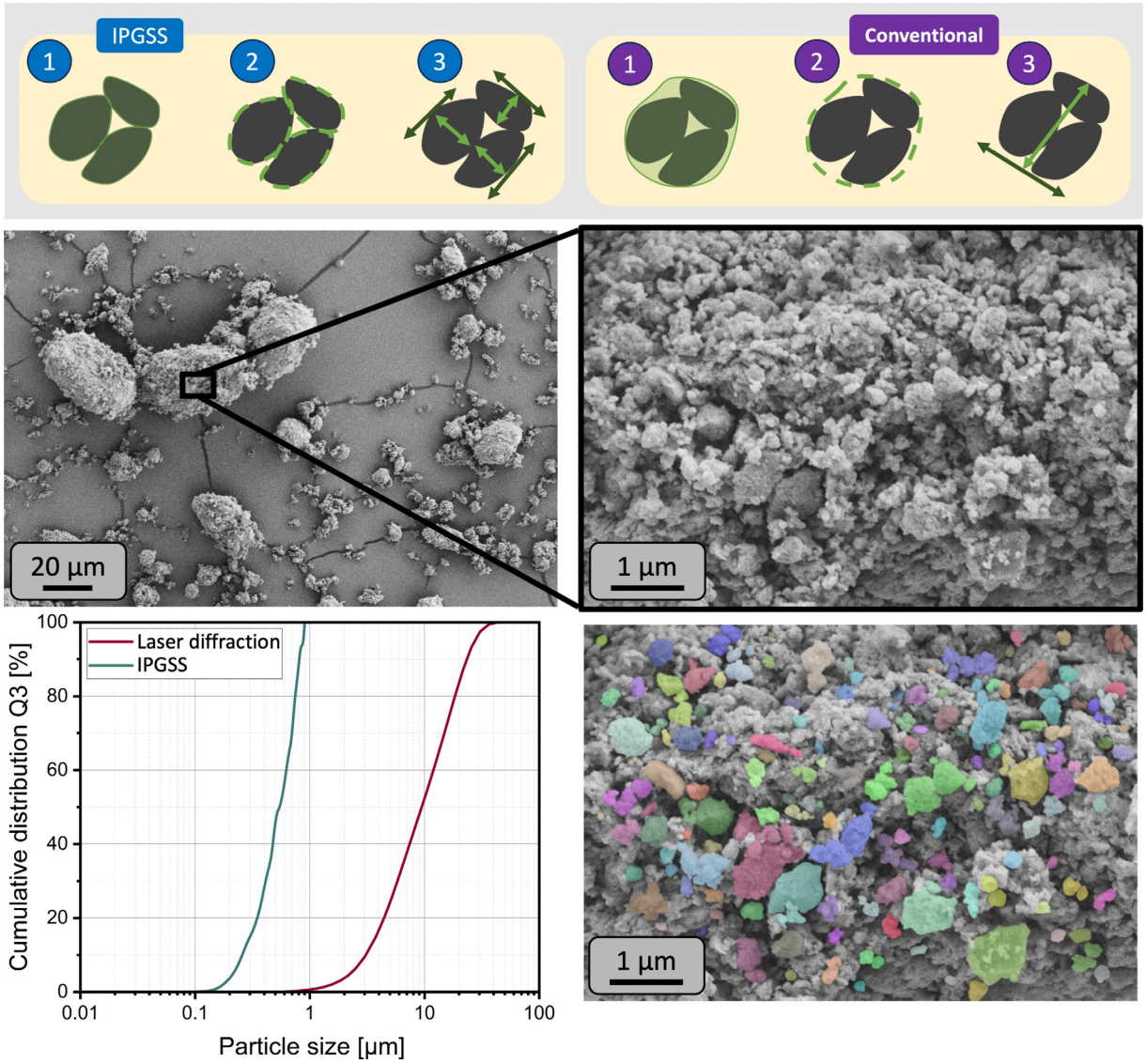

Fig. 5. Solid-state battery case study. Top: conceptual comparison of IPGSS and conventional measurement approaches for agglomerated solid electrolyte powders, illustrating differences in how each method resolves (1) Particle Size, (2) Circularity, and (3) Aspect Ratio. Middle left: SEM overview of comminuted Li_3InCl_6 showing agglomerated clusters. Middle right: magnified view of one agglomerate revealing submicron primary particles. Bottom left: PSD comparison between laser diffraction (red, D_{50} = 9.47 µm measuring agglomerates) and pipeline manual mode analysis (green, D_{50} = 0.54 µm measuring primary particles). Bottom right: segmented SEM image of the analyzed LIC agglomerate with color-coded particle masks.

SSB composite cathode design therefore demands direct primary-particle imaging.

This capability is demonstrated using LIC, synthesized via a solvent-based route [31] and subsequently comminuted. As shown in Fig. 5 (top), the comminuted powder contains both small primary particles and larger agglomerated LIC clusters. Conventional wet laser diffraction of the resulting powder detected only the agglomerated clusters, yielding D_{50} = 9.47 μm (Fig. 5, bottom left).

Using the manual segmentation mode, the IPGSS identified and quantified the primary particles within a single LIC agglomerate (Fig. 5, bottom right). The resulting particle size distribution differs markedly from that obtained by conventional laser diffraction, with a median primary-particle size of D_{50} = 0.54 μm. This represents a 17.5-fold discrepancy with the laser diffraction measurement, which is critical for accurate electrode design since the SE particle size governs ionic conductivity, mechanical stability, and overall electrochemical behavior [31,42,43]. As SEM-based analysis here covered approximately 150 particles, results should be interpreted with this limited count in mind and validated with larger datasets for routine quantitative use.

4. Conclusion

This work presented the IPGSS, a transformer-based pipeline combining zero-shot SAM segmentation, interactive correction, ISO-compliant size and shape analysis, and single-image surface roughness estimation via DRCS.

Measurement accuracy was confirmed using certified 390 μm polystyrene standard particles, with ECD D50 deviating by −0.3% and Fmax by +0.1% from the certified value. Despite the intentionally challenging imaging conditions, number-weighted analysis of the nominal 50 μm material yielded D_{50} = 49.9 μm (−0.2%), and volume-weighted Q_3 D_{90} matched QICPIC reference measurements within 0.4 to 4%, with larger Q_3 D_{50} deviations as expected from volume weighting. Both datasets exceeded the minimum particle count requirements established by Masuda and Gotoh [27], and D_{50} and D_{90} percentile uncertainties of approximately 1% (D_{10}: 2.4–3.4%) confirmed adequate precision following the Matsuyama [28] framework.

The IPGSS outperformed both OpenCV (fragmented boundaries) and Cellpose (adjacent particles merged by 25 to 100%) on the same intentionally complex images. The hierarchical post-processing cascade achieved accurate segmentation across diverse conditions without domain-specific training, and the interactive hybrid workflow, in which users apply SAM-guided corrections after automatic segmentation, addresses a fundamental limitation of existing tools that produce fixed, uncorrectable outputs.

The DRCS contour roughness method (rms_rq) achieved Spearman r = 0.983 ($p < 0.001$) against the tilt-series reference of Hülagü et al. [19] on 17 nanoparticles, with RMSE = 1.48 nm for quality-ok particles (n = 6, circularity ≥ 0.80) and 96.3% of pairwise roughness rankings correctly preserved from a single zero-tilt SEM image, replacing their 6–10 tilt images and motorized stage. DRCS directly addresses the IsoData intensity thresholding that Hülagü et al. identified as their most critical uncertainty source, replacing it with zero-tuning SAM/SAM2 segmentation. A depth-derived sdr/snr ratio separated SiO_2-coated from uncoated particles with zero overlap; angular homogeneity and Spc further discriminated coating architecture, providing surface descriptors inaccessible to contour-only methods. A ∼20 nm MiDaS noise floor caused hemisphere Rq to overestimate by 1.1–6.8×, largest for smooth particles, though between-type ordering was correctly preserved (r = 0.775). A prospective quality flag further extends practical utility.

The solid-state battery case study demonstrated practical impact: the IPGSS manual mode resolved submicron primary particles (D_{50} = 0.54 μm) within agglomerated Li_3InCl_6 solid electrolyte structures that conventional laser diffraction measured at D_{50} = 9.47 μm, a 17.5-fold discrepancy critical for electrode microstructure design.

Future development should focus on three priorities: reducing the ∼20 nm MiDaS depth noise floor through a Shape-from-Shading (SfS) refinement stage that recovers high-frequency surface normals from the secondary-electron intensity gradient, enabling true areal roughness (Sq) from a single image; validation on a broader nanoparticle dataset to confirm generalizability of the contour roughness method and sdr/snr classifier; and extending the circularity bias-correction to a validated continuous function for routine use.

Declaration of Generative AI and AI-assisted technologies in the writing process

During the preparation of this work, the authors used DeepL, ChatGPT, and Claude to improve the readability of the language and to assist with data analysis and visualization. After using these tools, the authors reviewed and edited the content as needed and took full responsibility for the content of the publication.

CRediT authorship contribution statement

Ahmed Eisa: Writing – original draft, Visualization, Validation, Software, Methodology, Formal analysis, Data curation, Conceptualization. **Mayank Gupta:** Software, Data curation. **Alex Kong:** Software, Data curation. **Finn Frankenberg:** Validation, Data curation. **Maximilian Kissel:** Visualization, Validation, Data curation. **Dimitri Ivanov:** Validation, Data curation. **Kostas Giannis:** Methodology, Conceptualization. **Carsten Schilde:** Funding acquisition.

Declaration of competing interest

The authors declare that they have no known competing financial interests or personal relationships that could have appeared to influence the work reported in this paper.

Acknowledgments

The authors want to thank the Heisenberg Program SCHI 1265/19-1 “Digital methods for complex systems in process and production engineering”. The authors also gratefully acknowledge microParticles GmbH (Berlin, Germany) for providing the certified polystyrene size standard particles used for measurement validation in this work.

Appendix A. Supplementary data

Supplementary data to this article can be found online at https://doi.org/10.1016/j.apt.2026.105304.

References

[1] T. Allen, Particle size Measurement, 5th ed., Chapman and Hall, London, 1997.
[2] H.G. Merkus, Particle size Measurements: Fundamentals, Practice, Quality, Springer, Dordrecht, 2009.
[3] G. Eshel, G.J. Levy, U. Mingelgrin, M.J. Singer, Critical evaluation of the use of laser diffraction for particle-size distribution analysis, Soil Sci. Soc. Am. J. 68 (2004) 736–743.
[4] R. Xu, O.A. Di Guida, Comparison of sizing small particles using different technologies, Powder Technol. 132 (2003) 145–153.

[5] N. Otsu, A threshold selection method from gray-level histograms, IEEE Trans. Syst. Man Cybern. 9 (1979) 62–66.
[6] L. Vincent, P. Soille, Watersheds in digital spaces: an efficient algorithm based on immersion simulations, IEEE Trans. Pattern Anal. Mach. Intell. 13 (1991) 583–598.
[7] G. Bradski, The OpenCV library, Dr. Dobb's J. Softw. Tools 25 (2000) 120–125.
[8] O. Ronneberger, P. Fischer, T. Brox, U-Net: convolutional networks for biomedical image segmentation, in: Int. Conf. Med. Image Comput. Comput.-Assist. Interv., Springer, 2015, pp. 234–241.
[9] K. He, G. Gkioxari, P. Dollár, R. Girshick, Mask R-CNN, in: IEEE Int. Conf. Comput. Vis., 2017, pp. 2961–2969.
[10] C. Stringer, T. Wang, M. Michaelos, M. Pachitariu, Cellpose: a generalist algorithm for cellular segmentation, Nat. Methods 18 (2021) 100–106.
[11] R. Bommasani, D.A. Hudson, E. Adeli, et al., On the opportunities and risks of foundation models, arXiv:2108.07258 (2021).
[12] A. Kirillov, E. Mintun, N. Ravi, H. Mao, C. Rolland, L. Gustafson, T. Xiao, S. Whitehead, A.C. Berg, W.Y. Lo, P. Dollár, R. Girshick, Segment Anything, in:, IEEE Int. Conf. Comput. vis. (2023) 4015–4026.
[13] A. Vaswani, N. Shazeer, N. Parmar, J. Uszkoreit, L. Jones, A.N. Gomez, Ł. Kaiser, I. Polosukhin, Attention is all you need, in, Adv. Neural Inf. Process. Syst. (2017) 5998–6008.
[14] A. Dosovitskiy, L. Beyer, A. Kolesnikov, D. Weissenborn, X. Zhai, T. Unterthiner, M. Dehghani, M. Minderer, G. Heigold, S. Gelly, J. Uszkoreit, N. Houlsby, An image is worth 16x16 words: transformers for image recognition at scale, in: Int. Conf. Learn. Represent., 2021.
[15] A. Archit et al., Segment anything for microscopy, Nat. Methods 22 (2025) 579–591.
[16] R. Larsen, T.L. Villadsen, J.K. Mathiesen, K.M.Ø. Jensen, E.D. Bøjesen, NP-SAM: implementing the Segment Anything Model for easy nanoparticle segmentation in electron microscopy images, ChemRxiv (2023). https://doi.org/10.26434/chemrxiv-2023-k73qz-v2.
[17] G.A.A. Monteiro, B.A.A. Monteiro, J.A. dos Santos, A. Wittemann, Pre-trained artificial intelligence-aided analysis of nanoparticles using the segment anything model, Sci. Rep. 15 (2025) 2341.
[18] L. Rettenberger, N.J. Szymanski, Y. Zeng, et al., Uncertainty-aware particle segmentation for electron microscopy at varied length scales, npj Comput, Mater 10 (2024) 124.
[19] D. Hülagü, C. Tobias, R. Dao, P. Komarov, K. Rurack, V.D. Hodoroaba, Towards 3D determination of the surface roughness of core-shell microparticles as a routine quality control procedure by scanning electron microscopy, Sci. Rep. 14 (2024) 17936.
[20] R. Ranftl, A. Bochkovskiy, V. Koltun, Vision transformers for dense prediction, in: IEEE Int. Conf. Comput. Vis., 2021, pp. 12179–12188.
[21] R. Ranftl, K. Lasinger, D. Hafner, K. Schindler, V. Koltun, Towards robust monocular depth estimation: mixing datasets for zero-shot cross-dataset transfer, IEEE Trans. Pattern Anal. Mach. Intell. 44 (2022) 1623–1637.
[22] Iso, Representation of Results of Particle Size Analysis - Part 6: Descriptive and Quantitative Representation of Particle Shape and Morphology 9276–6: (2008) 2008.
[23] Iso, Particle Size Analysis - Image Analysis Methods - Part 1: Static Image Analysis Methods 13322–1: (2014) 2014.
[24] Iso, Geometrical product specifications (GPS) - Surface texture: profile method - terms, Definitions and Surface Texture Parameters, 4287, International Organization for Standardization, Geneva, 1997, p. 1997.
[25] Iso, Geometrical product specifications (GPS) - Surface texture: profile method -, Rules and Procedures for the Assessment of Surface Texture, 4288, International Organization for Standardization, Geneva, 1996, p. 1996.
[26] S. GmbH, QICPIC - dynamic image analysis, Tech. Document. (2020).
[27] H. Masuda, K. Gotoh, Study on the sample size required for the estimation of mean particle diameter, Adv. Powder Technol. 10 (1999) 159–173.
[28] T. Matsuyama, Estimation of uncertainty of percentile values in particle size distribution analysis as a function of number of particles, Adv. Powder Technol. 30 (2019) 2616–2619.
[29] Iso, Particle Size Analysis - Image Analysis Methods - Part 2: Dynamic Image Analysis Methods 13322–2: (2006) 2006.
[30] microParticles GmbH, NIST- and IRMM-traceable Polystyrene Particle Size Standards, microParticles GmbH, Volmerstr. 9A, D-12489 Berlin, Germany, https://microparticles.de.
[31] F. Frankenberg, M. Kissel, C.F. Burmeister, M. Lippke, J. Janek, A. Kwade, Investigating the production of all-solid-state battery composite cathodes by numerical simulation of the stressing conditions in a high-intensity mixer, Powder Technol. 435 (2024) 119403.
[32] N. Ravi, V. Gabeur, Y.-T. Hu, R. Hu, C. Ryali, T. Zhang, A. Roller, G. Pavlakos, A. Berg, R. Girshick, P. Dollár, C. Feichtenhofer, SAM 2: Segment Anything in Images and Videos, arXiv:2408.00714 (2024).
[33] Iso, Representation of Results of Particle Size Analysis - Part 1: Graphical Representation 9276–1: (2014) 1998.
[34] Iso, Representation of Results of Particle Size Analysis - Part 2: Calculation of Average Particle Sizes/diameters and Moments from Particle Size Distributions 9276–2: (2014) 2014.
[35] J. Janek, W.G. Zeier, A solid future for battery development, Nat. Energy 1 (2016) 16141.
[36] S. Randau, D.A. Weber, O. Kötz, R. Koerver, P. Braun, A. Weber, E. Ivers-Tiffée, T. Adermann, J. Kulisch, W.G. Zeier, F.H. Richter, J. Janek, Benchmarking the performance of all-solid-state lithium batteries, Nat. Energy 5 (2020) 259–270.
[37] F. Frankenberg, C.A. Heck, M. Kissel, M.A. Lange, V. Faka, A. Diener, P. Haase, P. Michalowski, W.G. Zeier, J. Janek, A. Kwade, Tailoring composite microstructure through milling for dry-processed sulfide-based solid-state battery cathodes, Small 21 (2025) e07279. https://doi.org/10.1002/smll.202507279.
[38] A.P. Tinke, R. Govoreanu, I. Weuts, K. Vanhoutte, D. De Smaele, A review of underlying fundamentals in a wet dispersion size analysis of powders, Powder Technol. 196 (2009) 102–114.
[39] S. Jaffari, B. Forbes, E. Collins, D. Barlow, G.P. Martin, D. Murnane, Rapid characterization of the inherent dispersibility of respirable powders using dry dispersion laser diffraction, Int. J. Pharm. 447 (2013) 124–131.
[40] J. Ruhl, L.M. Riegger, M. Ghidiu, W.G. Zeier, Impact of solvent treatment of the superionic argyrodite Li_6PS_5Cl on solid-state battery performance, Adv. Energy Sustainability Res. 2 (2021) 2000077.
[41] A. Tron, A. Paolella, A. Beutl, New insights of infiltration process of argyrodite Li_6PS_5Cl solid electrolyte into conventional lithium-ion electrodes for solid-state batteries, Batteries 9 (2023) 503.
[42] T. Shi, Q. Tu, Y. Tian, Y. Xiao, L.J. Miara, O. Kononova, G. Ceder, High active material loading in all-solid-state battery electrode via particle size optimization, Adv. Energy Mater. 10 (2020) 1902881.
[43] M. Clausnitzer, R. Mücke, F. Al-Jaljouli, S. Hein, M. Finsterbusch, T. Danner, D. Fattakhova-Rohlfing, O. Guillon, A. Latz, Optimizing the composite cathode microstructure in all-solid-state batteries by structure-resolved simulations, Batteries Supercaps 6 (2023) e202300167.